Journal of Power Sources 194 (2009) 794–800

Contents lists available at ScienceDirect

Journal of Power Sources

journal homepage: www.elsevier.com/locate/jpowsour

Studies of tin–transition metal–carbon and tin–cobalt–transition metal–carbon negative electrode materials prepared by mechanical attrition

P.P. Ferguson [a], M.L. Martine [a], A.E. George [a], J.R. Dahn [a,b,*]

[a] Department of Physics and Atmospheric Science, Dalhousie University, Halifax, NS, Canada B3H 3J5
[b] Institute for Research in Materials, Dalhousie University, Halifax, NS, Canada B3H 3J5

ARTICLE INFO

Article history:
Received 13 April 2009
Received in revised form 15 May 2009
Accepted 18 May 2009
Available online 23 May 2009

Keywords:
Negative electrode
Mechanical attrition
Tin–carbon alloys
Sn–Co–C
Lithium-ion batteries

ABSTRACT

Samples of $Sn_{30}TM_{30}C_{40}$ and of $Sn_{30}Co_{15}TM_{15}C_{40}$, with TM = 3d transition metals, were prepared by vertical-axis attritor milling. The structure and performance of these samples were studied by X-ray diffraction (XRD) and by electrochemical testing. The XRD patterns of $Sn_{30}TM_{30}C_{40}$ show an amorphous-like diffraction pattern only for the sample with TM = Co. The other prepared samples show broadened Bragg peaks of their main starting material, along with an amorphous-like background, even after 32 h of milling. Samples with TM = Co and TM = Ni show stable differential capacity versus potential plots and stable cycling for at least 100 cycles with reversible capacities of 425 and 250 mAh g^{-1}, respectively. All samples prepared with 15 at.% Co show good capacity retention for at least 100 cycles ranging from 270 mAh g^{-1} for samples with TM = Ni to 500 mAh g^{-1} for samples with TM = Ti. The differential capacity versus potential plots for all the prepared $Sn_{30}Co_{15}TM_{15}C_{40}$ samples show similar structure to that of $Sn_{30}Co_{30}C_{40}$ except when TM = Cu. This shows the possibility of preparing tin-based negative electrode materials using a combination of cobalt and TM, especially if one looks to reduce the cobalt content.

© 2009 Elsevier B.V. All rights reserved.

1. Introduction

Tin–transition metal–carbon (Sn–TM–C) alloys have been used to replace graphite as the negative electrode for lithium-ion batteries. The Sony Corporation launched in 2005 a lithium-ion battery that uses a "tin-based amorphous anode" comprising tin, cobalt and carbon as the negative electrode [1]. 3d transition metals have been the TM of choice due to their relatively small atomic weight and due to their many stable Sn–TM intermetallics. Out of the 3d transition metals, Todd et al. [2] showed by combinatorial sputtering methods that cobalt is the best choice as TM in the Sn–TM–C system. Sn and Co exhibit strong bonding, as evidenced by a number of stable intermetallic phases, while Sn–C and Co–C exhibit no binding or weak binding as evidenced by the existence of no Sn–C intermetallic phases and only metastable Co–C phases. Therefore, a mixture of Sn, Co and C atoms, prepared by sputtering or by mechanical milling methods naturally "self assemble" into Co–Sn grains in a carbon matrix, based on the interatomic interactions. The carbon matrix provides pathways for lithium ions and electrons to travel to the Co–Sn grains *and* prevents the aggregation of Sn into large grains during repeated cycling.

Ferguson et al. [3] showed that it was possible to prepare nanostructured $Sn_{30}Co_{30}C_{40}$ by mechanical attrition; an economical and industrially scalable technique. In that study, the combination of $CoSn_2$, Co and graphite powders as the starting materials showed a desirable nanostructured-type X-ray diffraction (XRD) pattern. One disadvantage in using such a high energy milling process is being unable to use elemental Sn powder as a starting material. Because of its low melting point, Sn powder has poor mechanical properties. If used, chunks of materials are formed in the attritor instead of a uniform powder. Therefore, the use of Sn-rich intermetallics is required to prepare suitable Sn–TM–C powder alloys by mechanical attriting.

In addition to several electrochemical studies done on Sn–Co–C negative electrode materials [2–10], there have been other studies on Sn–TM–C involving 3d transition metals: Ti [2], V [2], Fe [11–13], Ni [14], Mn [15] and Cu [16]. No studies to our knowledge were specifically made with TM = Sc, TM = Cr and TM = Zn. Scandium, a rare earth metal, would not be useful for commercial purposes due to its rarity and high price. There are no Sn–Zn, Sn–C nor Zn–C intermetallic phases so there is no reason for the desired nanostructure to form during mechanical attriting. Furthermore, Zn, like Sn is ductile so materials problems during milling can be expected. As for chromium, Todd et al. [17] studied the structural and electrochemical aspects of sputtered Sn–Cr alloys, but no Sn–Cr–C systems were studied electrochemically.

To prepare Sn–TM–C materials by high energy mechanical milling, one desires Sn–TM intermetallics rich in Sn. This would

* Corresponding author at: Dalhousie University, Department of Physics and Atmospheric Science, Sir James Dunn Building, Halifax, NS, Canada B3H 3J5.
Tel.: +1 902 494 2991; fax: +1 902 494 5191.
E-mail address: jeff.dahn@dal.ca (J.R. Dahn).

0378-7753/$ – see front matter © 2009 Elsevier B.V. All rights reserved.
doi:10.1016/j.jpowsour.2009.05.031

eliminate the need for additional elemental Sn as a starting material. According to equilibrium binary phase diagrams [18], the Sn-rich intermetallics for TM = V, Mn, Fe, Co, Ni and Cu are V_2Sn_3, $MnSn_2$, $FeSn_2$, $CoSn_2$, Ni_3Sn_4 and Cu_6Sn_5, respectively. A recent study on the Sn–Ti phase diagram includes a new stable intermetallic, Ti_2Sn_3, which is more Sn-rich than the one in previous phase diagrams, Ti_6Sn_5 [19]. There are no stable Sn–Cr intermetallics in the equilibrium phase diagram [20], making it difficult to prepare Sn–Cr–C alloys by mechanical milling. There have been reports of a metastable phase, Cr_2Sn_3, which decomposes irreversibly at 438 °C under vacuum [20]. The following paragraph is a brief review of the electrochemical properties of the Sn-rich Sn–TM intermetallics mentioned above.

No electrochemical results for V_2Sn_3 powder have been reported, but Yoshinaga et al. [21] prepared a Sn–V thin film alloy mainly composed of the V_2Sn_3 phase with a Sn impurity. An initial rechargeable capacity of 500 mAh g^{-1} with a capacity retention of 400 mAh g^{-1} after 50 charge–discharge cycles was observed for this Sn–V alloy [21]. Xue and Fu [22] obtained a reversible capacity of 467 mAh g^{-1} at the first recharge for $CrSn_2$ material prepared by pulsed laser deposition. In that work, the XRD peaks of $CrSn_2$ were described as those of metastable Cr_2Sn_3 [22]. Zhang and Xia [23] obtained a first recharge capacity of 650 mAh g^{-1} for milled $CoSn_2$. Without milling, a first recharge capacity of about 475 mAh g^{-1} was observed [23]. Larcher et al. [24] obtained a first recharge capacity of approximately 560, 610 and 575 mAh g^{-1} for crystalline powders of $MnSn_2$, $FeSn_2$ and $CoSn_2$, respectively. Lee et al. [25] prepared Ni_3Sn_4 by high energy ball milling. In that work, the sample milled for 10 h shows a relatively low first recharge capacity of 275 mAh g^{-1} [25]. Wang et al. [26] studied Cu_6Sn_5 prepared by high energy ball milling. A sample milled for 110 h had a first reversible capacity near 400 mAh g^{-1} [26]. To our knowledge, no electrochemical results for Ti_2Sn_3 have been reported in the literature.

In an attempt to reduce the amount of Co in $Sn_{30}Co_{30}C_{40}$, Ferguson et al. [13] showed that $Sn_{30}Co_{15}Fe_{15}C_{40}$ had very similar electrochemical performance to that of $Sn_{30}Co_{30}C_{40}$. The replacement of cobalt by iron would significantly reduce the cost of starting materials. Without concerns about material cost, would the substitution of Fe by another 3d transition metal in $Sn_{30}Co_{15}Fe_{15}C_{40}$ result in acceptable electrochemical results and even in a nanostructured-like XRD pattern? In this work, a vertical-axis attritor was used to prepare $Sn_{30}TM_{30}C_{40}$ for TM = Mn, Fe, Co, Ni and Cu, and to prepare $Sn_{30}Co_{15}TM_{15}C_{40}$ for TM = Ti, V, Cr, Mn, Fe, Ni and Cu. XRD was used to examine the structural features of the samples and electrochemical tests in Li/$Sn_{30}TM_{30}C_{40}$ and Li/$Sn_{30}Co_{15}TM_{15}C_{40}$ cells were made.

2. Experimental

$Sn_{30}TM_{30}C_{40}$ and $Sn_{30}Co_{15}TM_{15}C_{40}$ samples were alloyed mechanically using a vertical-axis attritor (Union Process 01-HD attritor). Due to the poor milling properties of starting materials containing elemental Sn powder, samples were prepared from Sn–TM intermetallics with the richest Sn content according to the binary phase diagrams. Table 1 shows these Sn–TM intermetallics along with their annealing preparation parameters. $Sn_{30}Cr_{30}C_{40}$ was not prepared since there are no stable Sn–Cr intermetallics [18]. Except for Ti_2Sn_3, all Sn–TM intermetallics were arc melted from elemental Sn and TM powders then subsequently annealed under flowing argon with the parameters indicated in Table 1. Ti_2Sn_3 was prepared by combining stoichiometric amounts of Ti sponge and Sn powder in an argon filled quartz ampoule [27]. The ampoule was then heated as indicated in Table 1. After annealing, all Sn–TM intermetallics were ground, coarse grains were removed using a 300 mesh sieve and the resulting powders were characterized by XRD. Stoichiometric amounts of graphite powder (Fluka, purum) and elemental TM powder were added to the samples to make up the starting charges for the attritor. The added elemental TM powders are indicated in Table 1, except for Ti (Sigma–Aldrich, −100 mesh, 99.7%) and for Ni powder (Fisher Chemical). A small amount of elemental Sn powder (Sigma–Aldrich, <150 μm, 99.5%) was added to Cu_6Sn_5 to reach the proper stoichiometric ratio and this Sn powder was incorporated into the alloy. $Sn_{30}Co_{15}TM_{15}C_{40}$ samples were prepared from a mixture of $CoSn_2$, Co, Sn–TM, TM and graphite. To prepare $Sn_{30}Co_{15}Cr_{15}C_{40}$, elemental Cr powder (Alfa Aesar, −100 mesh, 99%) was used along with $CoSn_2$ and graphite.

Details of material preparation and information on the mechanical attritor can be found in Reference [3]. Briefly, a powder charge of 25.0 g along with about 1400 1/4 in. diameter stainless steel balls were loaded into the 700 mL stainless steel attritor can and sealed under an argon atmosphere. The angular velocity of the shaft was set at 700 RPM for a total duration of 16 h or of 32 h. The resulting attrited powders were studied by XRD using a JD2000 diffractometer equipped with a Cu-target X-ray tube and a diffracted-beam monochromator. Each X-ray scan was collected from 20° to 60° in 0.05° increments at 30 s $point^{-1}$.

To characterize the attrited samples electrochemically, an electrode slurry was prepared by mixing 80 wt% attrited powder, 12 wt% Super-S carbon black (MMM Carbon, Belgium) and 8 wt% binder. The slurry was spread on Cu foil with a notch bar and dried at 90 °C for 4 h. The electrolyte used in all of the cells in this work was 1 M $LiPF_6$ in ethylene carbonate/diethyl carbonate [1:2 v/v] solution (Ferro Corp, Grant Chemical division) to which was added 10 wt% fluoroethylene carbonate (FEC) (Fujian ChuangXin, China). Choi et al. [28] showed that the addition of FEC to the electrolyte improves capacity retention and coulombic efficiency for a silicon thin film electrode. 2325 size coin-type cells with two Celgard 2300 separators and a lithium foil common counter and reference electrode were assembled in an argon-filled glove box using the electrodes described above.

For all cells, the same electrochemical testing protocol was used. After assembly, the coin cells were discharged from open circuit (near 2.7 V) to 0.005 V. The potential was then increased to 2.5 V to be decreased again to 0.005 V. This was done for a total of two cycles at a $C/10$ rate, as calculated prior from the expected theoretical capacity. After the first two cycles, the cells were discharged–charged from 0.005 to 1.2 V at a $C/5$ rate for 100 cycles.

3. Results and discussion

3.1. Studies of $Sn_{30}TM_{30}C_{30}$

Fig. 1 shows the XRD patterns of $Sn_{30}TM_{30}C_{40}$ for TM = Mn, Fe and Co. The diffraction pattern of the sample with TM = Co shows the typical Sn–Co–C two-hump pattern characteristic of nanometer sized amorphous CoSn grains in a carbon matrix [3,8,29]. A small amount of the main starting material, $CoSn_2$, is apparent in the sample milled for 16 h and is fully incorporated into the nanostructured component after 32 h of milling. A milling time significantly less than 16 h will result in prominent and sharper Bragg peaks of $CoSn_2$ [Fig. 1 in Ref. [3]]. Both diffraction patterns of the prepared $Sn_{30}Fe_{30}C_{40}$ samples show relatively broad Bragg peaks of $FeSn_2$. By using ^{57}Fe Mössbauer Effect spectroscopy, Ferguson et al. [13] showed that attrited $Sn_{30}Fe_{30}C_{40}$ has a significant amount of nanometer scale Fe-carbide in the alloy. This means that some of the elemental Fe added as starting material does not react directly with $FeSn_2$ as it is incorporated into the carbide, explaining why Bragg peaks of $FeSn_2$ are noticed. For the samples prepared with TM = Mn, the diffraction patterns of both samples show the Bragg peaks of its main starting materials, $MnSn_2$. No Mn-carbides are

Table 1
Annealing parameters of the Sn–TM intermetallics used as starting materials in this work.

Intermetallic	Transition metal source	Annealing temperature (°C)	Annealing time (h)
Ti_2Sn_3[a]	Alfa Aesar, 3–13 mm sponge, 99.95%	700	2 weeks [27]
V_2Sn_3	Alfa Aesar, −mesh, 99.5%	700	12
$MnSn_2$	Alfa Aesar, −140 + 325 mesh, 99.6%	500	24
$FeSn_2$	Alfa Aesar, <10 μm, 99.5%	490	70
$CoSn_2$	Sigma–Aldrich, <150 μm, 99.9 + %	500	24
Ni_3Sn_4	Sigma–Aldrich, 6–16 mm, 99.95 + %	700	12
Cu_6Sn_5	Alfa Aesar, −150 mesh, 99.5%	200	12

[a] Compound was not arc melted prior to annealing.

noticed by XRD. However, due to the same type of diffraction patterns as the ones with TM = Fe, it can be assumed that nanometer scale Mn-carbide or $SnMn_3C$ is possibly formed. The formation of carbide phases that are rich in transition metal, like Fe_3C, $Mn_{23}C_6$, $SnFe_3C$ and $SnMn_3C$, "remove" a higher fraction of transition metal than Sn from the desired $Sn_{30}TM_{30}C_{40}$ product, leading to the presence of $FeSn_2$ and $MnSn_2$ in the XRD patterns. Fig. 2 shows the XRD patterns of $Sn_{30}TM_{30}C_{40}$ with TM = Ni and TM = Cu. All XRD patterns show the Bragg peaks of the main starting materials, Ni_3Sn_4 or Cu_6Sn_5 for TM = Ni and TM = Cu, respectively, with broader Bragg peaks depicted for $Sn_{30}Ni_{30}C_{40}$ sample. A small amount of elemental Sn was added to prepare the sample with TM = Cu. The resulting $Sn_{30}Cu_{30}C_{40}$ powder was well milled and uniform, indicating that Sn was well incorporated into the alloy. There are no indications of elemental Ni in both $Sn_{30}Ni_{30}C_{40}$ XRD patterns. There are neither Ni nor Cu carbides [18].

Samples of $Sn_{30}TM_{30}C_{40}$ with TM = Ti and TM = V were prepared using Ti_2Sn_3 or V_2Sn_3 as the main starting materials. Independent of milling time, both alloys showed poor mechanical properties with non-uniform alloyed chunks as the resulting material. XRD patterns of these materials showed strong Bragg peaks of crystalline Sn. The precipitation of elemental Sn was observed by O'Brien et al. [30] when Ti_2Sn_3 was ball milled. Given the similarity between the Ti–Sn [Fig. 2 in Ref. [19]] and the V–Sn [18] binary phase diagrams near 60 at.% Sn, the precipitation of elemental Sn is expected and is observed for V_2Sn_3. If Sn–Ti–C or Sn–V–C alloys are to be prepared by mechanical milling techniques, starting materials, atomic ratios and/or milling parameters need to be more thoroughly investigated.

Fig. 3 shows the specific capacity versus charge–discharge cycle number for the electrodes in Li/$Sn_{30}TM_{30}C_{40}$ cells. All samples, except those of TM = Co and TM = Ni, show a decrease in specific capacity with cycle number. This is likely due to the presence of crystalline components as noted previously in their respective XRD patterns. Both $Sn_{30}Co_{30}C_{40}$ samples show stable capacity near 425 mAh g^{-1} while both $Sn_{30}Ni_{30}C_{40}$ samples show a lower, but stable capacity near 250 mAh g^{-1} for at least 100 cycles. Todd et al. [17] reported that sputtered $Sn_{1-x}Ni_x$ for $0 < x < 0.7$ showed a very small first recharge capacity (removing lithium from the alloy), consistent with that observed here. Naille et al. [31] described the first discharge (515 mAh g^{-1}) of crystalline Ni_3Sn_4 as a reaction of Li with Sn to form Li_7Sn_2 instead of $Li_{22}Sn_5$. However, the authors did not comment on the observed low first recharge capacity of only 286 mAh g^{-1}.

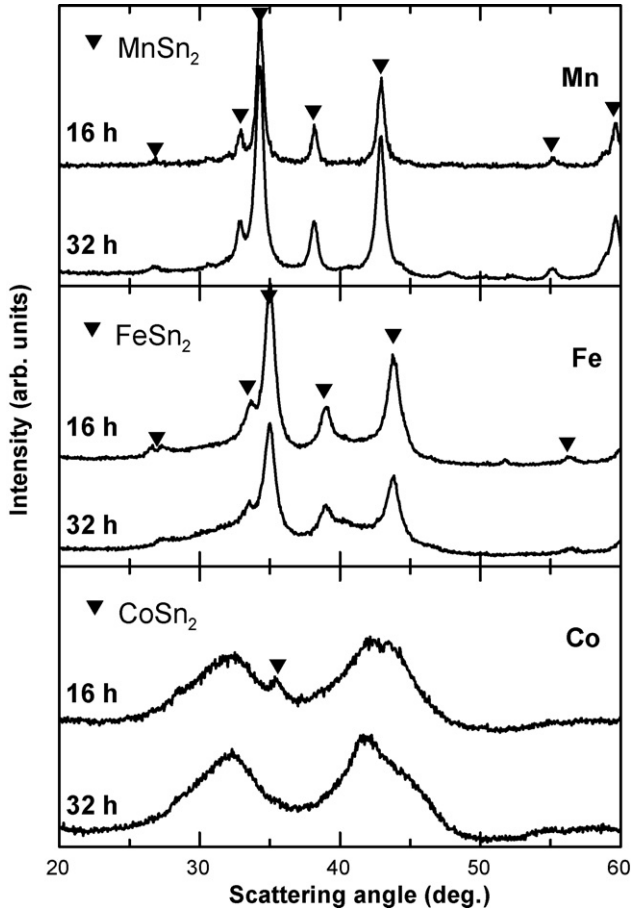

Fig. 1. X-ray diffraction patterns of $Sn_{30}TM_{30}C_{40}$ samples prepared by vertical-axis attritor milling for TM = Mn, Fe and Co. The milling time is indicated next to each curve. The Bragg peaks of $MnSn_2$, $FeSn_2$ and of $CoSn_2$ were observed and are indicated for reference.

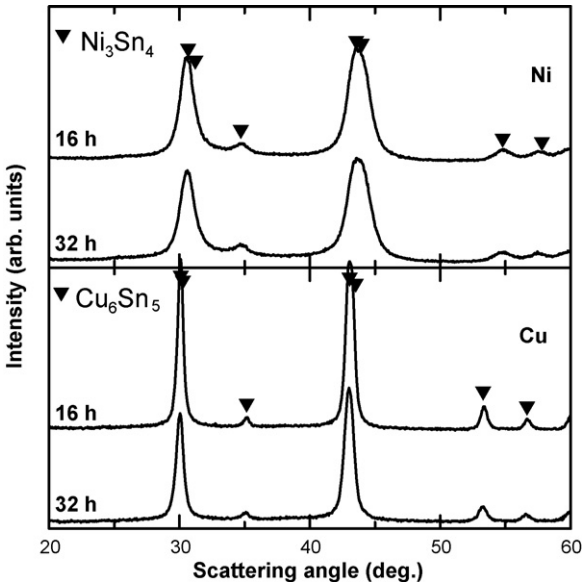

Fig. 2. X-ray diffraction patterns of $Sn_{30}TM_{30}C_{40}$ samples prepared by vertical-axis attritor milling for TM = Ni and Cu. The milling time is indicated next to each curve. The Bragg peaks of Ni_3Sn_4 and of Cu_6Sn_5 were observed and are indicated for reference.

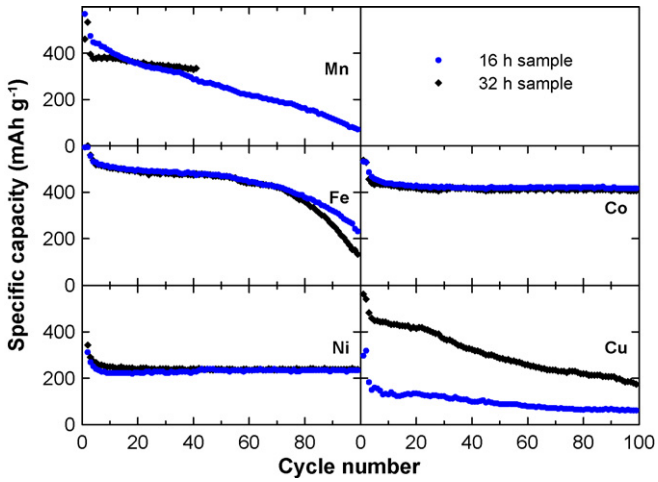

Fig. 3. Specific capacity versus cycle number for the samples described by Figs. 1 and 2 when incorporated in Li/$Sn_{30}TM_{30}C_{40}$ cells. Cells were charged and discharged between 0.005 and 2.5 V for the first two cycles at *C*/10. The following cycles were made between 0.005 and 1.2 V at *C*/5. Testing was done at 30 °C.

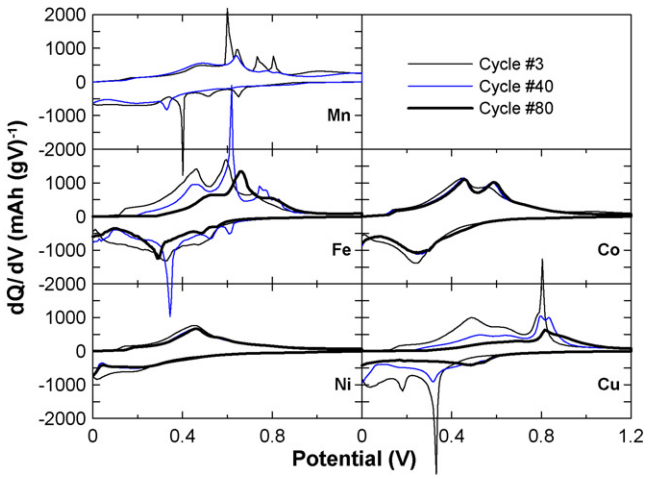

Fig. 5. Differential capacity versus potential for the electrochemical cells described by Fig. 3 (32 h samples). The value of TM in $Sn_{30}TM_{30}C_{40}$ is indicated next to each curve. The thin black lines show cycle 3, the thin coloured lines show cycle 40 and the bold black lines show cycle 80.

Fig. 4 shows the first recharge and the 10th recharge capacities observed for the $Sn_{30}TM_{30}C_{30}$ samples milled for 32 h. The expected theoretical capacity is indicated for each sample. The theoretical capacity was calculated based on the full lithiation of Sn, 4.4 Li atoms per Sn atom, and on the reaction of 0.5 Li atom per C atom [4]. Many forms of disordered carbon, including high energy ball-milled graphite [32], can react with up to 0.5 Li per carbon. The first recharge data was taken from 0.005 to 2.5 V while the 10th recharge data was taken from 0.005 to 1.2 V. The sample with TM = Fe shows the highest capacity while the sample with TM = Ni shows the lowest capacity. Fig. 5 shows the differential capacity versus potential for the $Sn_{30}TM_{30}C_{30}$ samples milled for 32 h. Samples with TM = Mn and with TM = Fe show features near 0.5, 0.7 and 0.8 V (during recharge) typically observed for crystalline Sn aggregation [33]. The sample with TM = Cu shows strong features near 0.8 V at recharge. This was previously attributed to the two phase region between a Li_2CuSn-type phase and Cu_6Sn_5, as it was observed in crystalline Cu_6Sn_5 by Larcher et al. [34]. Samples with TM = Co and with TM = Ni show stable d*Q*/d*V* plots with cycling and do not show sharp features characteristic of a two phase region. These aspects are typical of samples with excellent capacity retention. The other samples do not show stable d*Q*/d*V* plots with cycling which indicates atomic scale rearrangements normally accompanied with poor cycling capability. The differential capacities plots of $Sn_{30}Ni_{30}C_{40}$ show a single hump near 0.45 V.

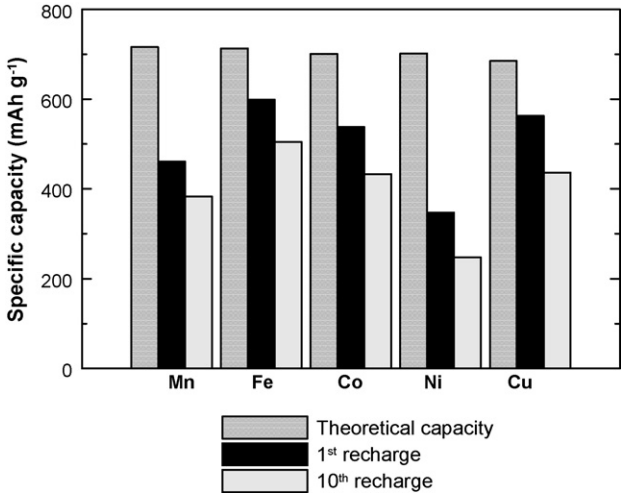

Fig. 4. Specific capacity versus TM in $Sn_{30}TM_{30}C_{40}$ for the samples milled for 32 h described in Fig. 3. Data was measured at the end of the first recharge (removing lithium) to 2.5 V and at the end of the 10th recharge to 1.2 V. The theoretical capacity is a calculation assuming each Sn and C atom can react with 4.4 and 0.5 Li atoms [4], respectively.

3.2. Studies of $Sn_{30}Co_{15}TM_{15}C_{30}$

Fig. 6 shows XRD patterns of $Sn_{30}Co_{15}TM_{15}C_{40}$ samples with TM = Ti, V, Ni and Cu. Strong features from $CoSn_2$ are present in samples with TM = Ti and TM = V while they are not present in samples with TM = Ni and with TM = Cu. For samples with TM = Ti and TM = V, a broad hump between 25° and 45° likely corresponds to an amorphous or nanostructured Sn–TM component. Unlike the preparation of $Sn_{30}TM_{30}C_{40}$, samples prepared with TM = Ti and V in $Sn_{30}Co_{15}TM_{15}C_{40}$ were very uniform and powdery which is likely due to the relatively small amount of Ti_2Sn_3 and V_2Sn_3 used, respectively. A broad feature near 40°–41° was present in the sample with TM = V milled for 16 h and was attributed to V_2C. XRD patterns for the samples prepared with Ni and Cu show broader Ni_3Sn_4 and Cu_6Sn_5 peaks, respectively, than those prepared without Co (Fig. 2). For samples with TM = Ti and TM = V, the elemental Co added as a starting material can alloy with the extra elemental TM to form stable Co–TM intermetallics [18]. No Bragg peaks of these intermetallics were observed. Fig. 7 shows the XRD pattern of $Sn_{30}Co_{15}TM_{15}C_{40}$ samples with TM = Cr, Mn and Fe. Both samples prepared with TM = Cr show a sharp peak of crystalline Cr which indicates that Cr does not mix well with $CoSn_2$ and carbon, at least for 32 h of milling. In addition, stable chromium carbides exist [18]. Since $MnSn_2$, $FeSn_2$ and $CoSn_2$ are isostructural [35], it is not simple to distinguish between their Bragg peaks. Samples of $Sn_{30}Co_{15}TM_{15}C_{40}$ milled for 32 h with TM = Mn and TM = Fe show almost the same nanostructured two hump diffraction pattern observed for $Sn_{30}Co_{30}C_{40}$. This can be attributed to Al_2Cu-type starting materials and to the full alloying of $CoSn_2$ with the elemental Co added as starting materials. Using ^{119}Sn and ^{57}Fe Mossbauer Effect spectroscopy, Ferguson et al. [13] showed that a $Sn_{30}Co_{15}Fe_{15}C_{40}$ sample milled for 16 h contained $FeSn_2$, Fe-carbide and nanostructured CoSn. Due to similar XRD pattern to that of $Sn_{30}Co_{15}TM_{15}C_{40}$ with TM = Fe, it can be assumed that nanostructured CoSn is also formed in the $Sn_{30}Co_{15}Mn_{15}C_{40}$ sample milled for 32 h.

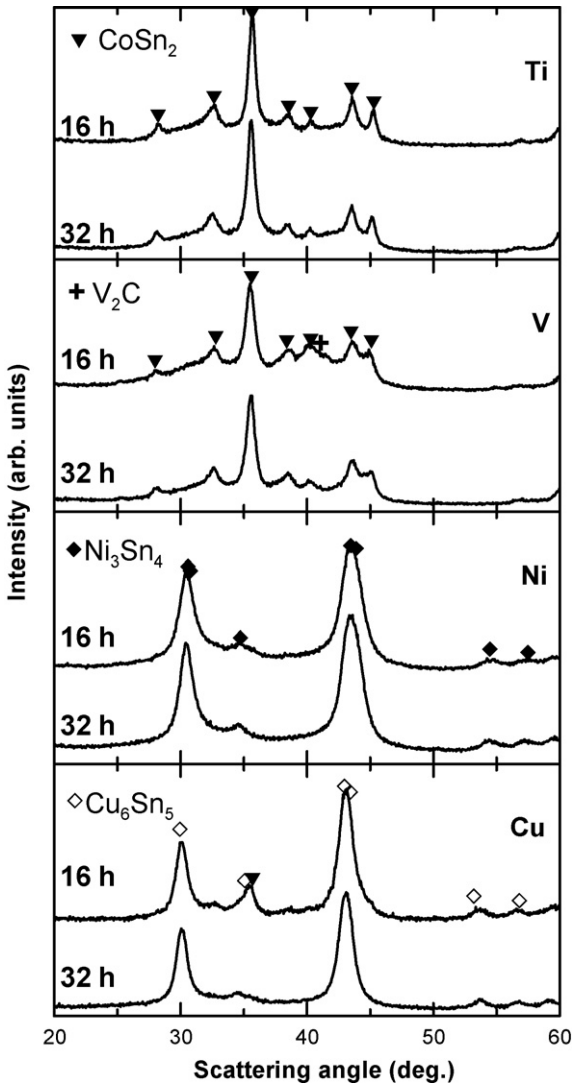

Fig. 6. X-ray diffraction patterns of $Sn_{30}Co_{15}TM_{15}C_{40}$ samples prepared by vertical-axis attritor milling for TM = Ti, V, Ni and Cu. The milling time is indicated next to each curve. The Bragg peaks of $CoSn_2$, V_2C, Ni_3Sn_4 and Cu_6Sn_5 were observed and are indicated for reference.

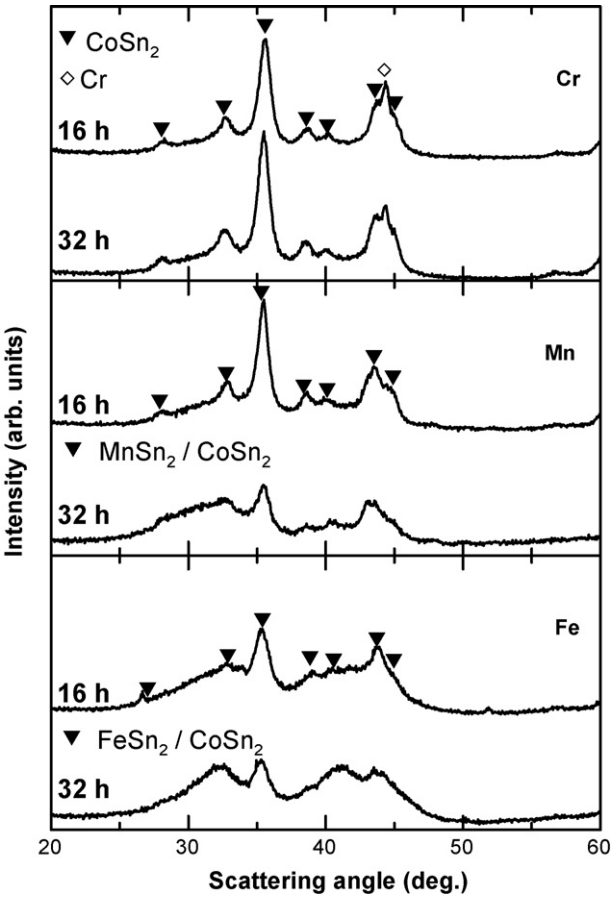

Fig. 7. X-ray diffraction patterns of $Sn_{30}Co_{15}TM_{15}C_{40}$ samples prepared by vertical-axis attritor milling for TM = Cr, Mn and Fe. The milling time is indicated next to each curve. The Bragg peaks of $CoSn_2$, Cr, $MnSn_2$ and $FeSn_2$ were observed and are indicated for reference.

Fig. 8 shows the specific capacity versus charge–discharge cycle number for the electrodes in Li/$Sn_{30}Co_{15}TM_{15}C_{40}$ cells. Stable cycling is observed for most of the samples, except for the samples milled for 32 h with TM = Ti and TM = Cu where a decrease in capacity is noticed towards the end of the cycles tested. Fig. 9 shows the first recharge, 10th recharge and theoretical capacities of electrochemical cells described by Fig. 8 (32 h samples only). The sample of $Sn_{30}Co_{30}C_{40}$ was added as reference. Again, it can be noticed that sample with TM = Ni shows the lowest capacity of the studied samples, but its capacity is slightly higher than when prepared without Co ($Sn_{30}Ni_{30}C_{40}$).

Fig. 10 shows differential capacity versus potential for the Li/$Sn_{30}Co_{15}TM_{15}C_{30}$ electrochemical cells (samples milled for 32 h). The dQ/dV plots for samples with TM = Fe and TM = Mn show features of Sn aggregation, notably for cycle number 80. All other samples show little to no changes between cycle 40 and 80 without any sharp features. The dQ/dV plots of samples with TM = Ti, V, Cr and Ni show the typical two hump feature in the recharge region normally noticed for nanostructured $Sn_{30}Co_{30}C_{40}$ (Fig. 3). The dQ/dV plot for cycle 3 of the sample with TM = Ni shows a single broad peak, as was previously observed in Fig. 5. The dQ/dV plots

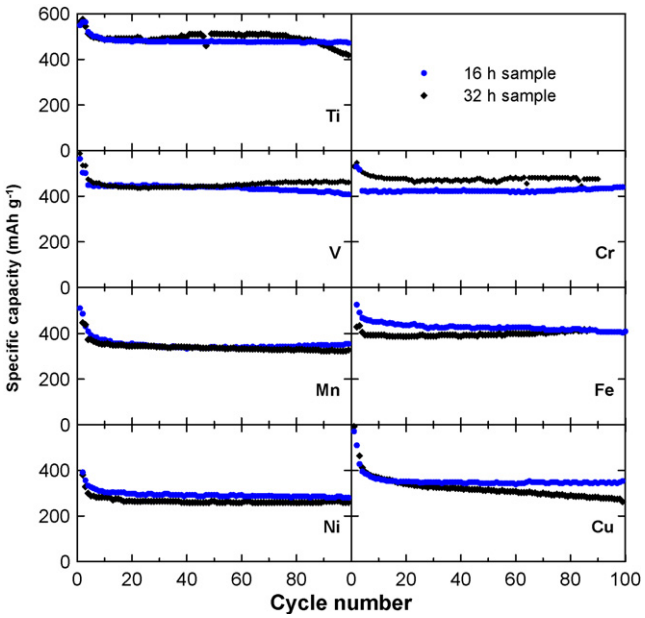

Fig. 8. Specific capacity versus cycle number for the samples described by Figs. 6 and 7 when incorporated in Li/$Sn_{30}Co_{15}TM_{15}C_{40}$ cells. Cells were charged and discharged between 0.005 and 2.5 V for the first two cycles at C/10. The following cycles were made between 0.005 and 1.2 V at C/5. Testing was done at 30 °C.

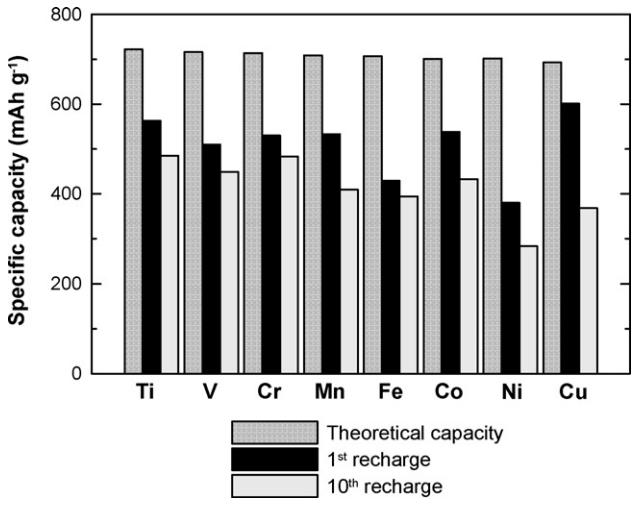

Fig. 9. Specific capacity versus TM in $Sn_{30}Co_{15}TM_{15}C_{40}$ for the samples milled for 32 h described in Fig. 8. The specific capacity of a Li/$Sn_{30}Co_{30}C_{40}$ cell was added for reference. Data was measured at the end of the first recharge (removing lithium) to 2.5 V and at the end of the 10th recharge to 1.2 V. The theoretical capacity is a calculation assuming each Sn and C atom can react with 4.4 and 0.5 Li atoms, respectively.

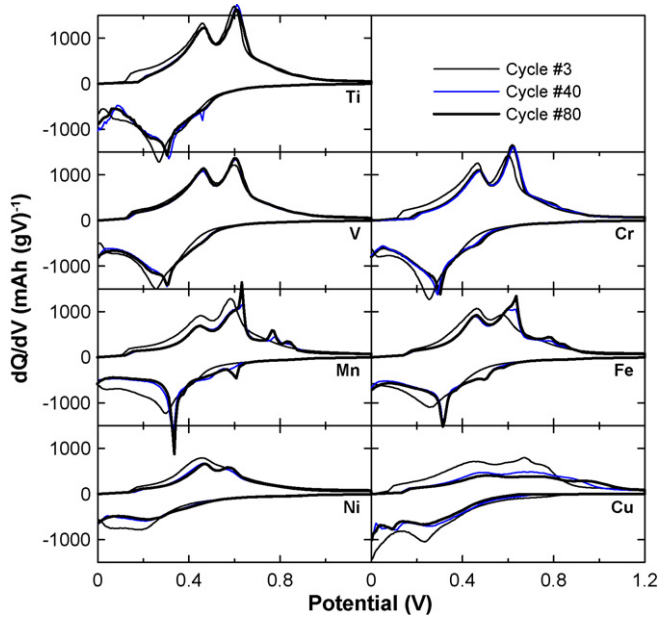

Fig. 10. Differential capacity versus potential for the electrochemical cells described by Fig. 8 (32 h samples). The value of TM in $Sn_{30}Co_{15}TM_{15}C_{40}$ is indicated next to each curve. The thin black lines show cycle 3, the thin coloured lines show cycle 40 and the bold black lines show cycle 80.

for the sample with TM = Cu show more capacity at higher potential than the other samples, but less than in $Sn_{30}Cu_{30}C_{40}$.

4. Conclusions

$Sn_{30}TM_{30}C_{40}$ and $Sn_{30}Co_{15}TM_{15}C_{40}$ alloys were prepared using a vertical-axis attritor. The samples were prepared using Sn-rich Sn–TM intermetallics. The samples were studied structurally and electrochemically. Out of the five $Sn_{30}TM_{30}C_{40}$ samples prepared, only the samples with TM = Co showed the desired nanostructured-type XRD pattern. Samples with TM = Co and TM = Ni had excellent capacity retention for at least 100 cycles at around 425 and 250 mAh g^{-1}, respectively. It is reasonable to explain the poor cycling behaviour of the other samples due to the presence of crystalline phases.

All samples prepared in the $Sn_{30}Co_{15}TM_{15}C_{40}$ series showed very acceptable stable capacity retention for at least 100 cycles. After 32 h of milling, samples with TM = Fe and TM = Mn were the only samples with a potentially nanostructured-type XRD pattern. However, the differential capacities of both samples showed evidence of Sn aggregation, which suggests capacity loss should occur after cycle 100. All electrochemical cells made with Ni in this work showed excellent capacity retention with low specific capacity. More work is needed to understand this unique behaviour among the TM tested.

The Sn–Co–C system has been proposed to be the best choice among Sn–TM–C for negative electrodes in Li-ion batteries since a nanostructure consisting of amorphous CoSn grains in a carbon matrix is formed during sputtering or during mechanical milling [2,3,8]. By replacing some of the Co with another TM, we showed that it is still possible to prepare materials with high capacity and stable cycling. Further work is needed to optimize the composition and the synthesis method, with an eye to cost reduction, improvement in specific capacity and increases in cycle life. It is very likely that the Sn–TM–C electrodes materials that show good capacity retention would also show good capacity retention in electrolytes based on propylene carbonate, instead of ethylene carbonate. This should be tested in future work.

Acknowledgements

The authors thank 3M Canada Co. and NSERC for funding this work under the auspices of the Industrial Research Chairs program.

References

[1] http://www.sony.net/SonyInfo/News/Press/200502/05-006E/.
[2] A.D.W. Todd, R.E. Mar, J.R. Dahn, J. Electrochem. Soc. 154 (2007) A597.
[3] P.P. Ferguson, A.D.W. Todd, J.R. Dahn, Electrochem. Commun. 10 (2008) 25.
[4] J.R. Dahn, R.E. Mar, Alyaa Abouzeid, J. Electrochem. Soc. 153 (2006) A361.
[5] J. Hassoun, S. Panero, G. Mulas, B. Scrosati, J. Power Sources 171 (2007) 928.
[6] G.F. Ortiz, R. Alcántara, I. Rodríguez, J.L. Tirado, J. Electroanal. Chem. 605 (2007) 98.
[7] R.B. Lewis, A. Timmons, R.E. Mar, J.R. Dahn, J. Electrochem. Soc. 154 (2007) A213.
[8] P.P. Ferguson, J.R. Dahn, Electrochem. Solid-State Lett. 11 (2008) A187.
[9] Z. Chen, J. Qian, X. Ai, Y. Cao, H. Yang, J. Power Sources 189 (2009) 730.
[10] S.-Il Lee, S. Yoon, C.-Min Park, Jae-M. Lee, H. Kim, D. Im, S.-G. Doo, Hun-J. Sohn, Electrochim. Acta 54 (2008) 364.
[11] O. Mao, R.A. Dunlap, J.R. Dahn, J. Electrochem. Soc. 146 (1999) 405.
[12] O. Mao, J.R. Dahn, J. Electrochem. Soc. 146 (1999) 423.
[13] P.P. Ferguson, Peng Liao, R.A. Dunlap, J.R. Dahn, J. Electrochem. Soc. 156 (2009) A13.
[14] H. Guo, H. Zhao, X. Jia, Electrochem. Commun. 9 (2007) 2207.
[15] L.Y. Beaulieu, J.R. Dahn, J. Electrochem. Soc. 147 (2000) 3237.
[16] N. Jayaprakash, N. Kalaiselvi, C.H. Doh, J. Appl. Electrochem. 37 (2007) 567.
[17] A.D.W. Todd, R.E. Mar, J.R. Dahn, J. Electrochem. Soc. 153 (2006) A1998.
[18] ASM International's Binary Alloy Phase Diagrams, second ed., Materials Park, OH 44073-0002, USA, 1990.
[19] F. Yin, J.-C. Tedenac, F. Gascoin, CALPHAD 31 (2007) 370.
[20] L. Hollan, P. Lecocq, C. R. Acad. Sci. Paris 262 (1966) 1577.
[21] H. Yoshinaga, S. Dan, A. Kawabata, T. Sakai, J. Jpn. Inst. Met. 66 (2002) 861.
[22] M.-Z. Xue, Z.-W. Fu, Solid State Ionics 177 (2006) 1501.
[23] J. Zhang, Y. Xia, J. Electrochem. Soc. 153 (2006) A1466.
[24] D. Larcher, L.Y. Beaulieu, O. Mao, A.E. George, J.R. Dahn, J. Electrochem. Soc. 147 (2000) (1703).
[25] H.-Y. Lee, S.-W. Jang, S.-M. Lee, S.-J. Lee, H.-K. Baik, J. Power Sources 112 (2002) 8.
[26] G.X. Wang, L. Sun, D.H. Bradhurst, S.X. Dou, H.K. Liu, J. Alloy Compd. 299 (2000) L12.
[27] J.W. O'Brien, R.A. Dunlap, J.R. Dahn, J. Alloy Compd. 353 (2003) 60.
[28] N.-S. Choi, K.H. Yew, K.Y. Lee, M. Sung, Ho Kim, S.-S. Kim, J. Power Sources 161 (2006) 1254.
[29] A.D.W. Todd, R.A. Dunlap, J.R. Dahn, J. Alloys Compd. 443 (2007) 114.
[30] J.W. O'Brien, R.A. Dunlap, J.R. Dahn, J. Alloys Compd. 353 (2003) 65.

[31] S. Naille, C.M. Ionica-Bousquet, F. Robert, F. Morato, P.-E. Lippens, J. Olivier-Fourcade, J. Power Sources 174 (2007) 1091.
[32] F. Disma, L. Aymard, L. Dupont, J.M. Tarascon, J. Electrochem. Soc. 143 (1996) 3959.
[33] I.A. Courtney, J.R. Dahn, J. Electrochem. Soc. 144 (1997) 2045.
[34] D. Larcher, L.Y. Beaulieu, D.D. MacNeil, J.R. Dahn, J. Electrochem. Soc. 147 (2000) 1658.
[35] P. Villars, L.D. Calvert, Pearson's Handbook of Crystallographic Data for Intermetallic Phases, second ed., ASM International, 1991.